A concentrated $AlCl_3$–diglyme electrolyte for hard and corrosion-resistant aluminum electrodeposits

Zelei Zhang,[a,b] Atsushi Kitada,[a,*] Si Gao,[a] Kazuhiro Fukami,[a] Nobuhiro Tsuji,[a] Zhengjun Yao,[b] and Kuniaki Murase[a]

[a] Department of Materials Science and Engineering, Kyoto University, Kyoto 606-8501, Japan

[b] College of Materials Science and Technology, Nanjing University of Aeronautics and Astronautics, Nanjing 210016, China

[*]Corresponding Author

E-mail address: kitada.atsushi.3r@kyoto-u.ac.jp (A. Kitada)

Abstract

A concentrated aluminum chloride ($AlCl_3$)–diglyme (G2) electrolyte is used to prepare hard and corrosion-resistant aluminum (Al) electrodeposited films. The Al electrodeposits obtained from the electrolyte with $AlCl_3$/G2 molar ratio $x = 0.4$ showed a void-free microstructure composed of spherical particles, in stark contrast to flake-like morphologies with micro-voids for lower x. Neutral complex rarely exists in the $x = 0.4$ electrolyte, resulting in a relatively high conductivity despite the high concentration and high viscosity. Nanoindentation measurements for the Al deposits with >99% purity revealed that the nano-hardness was 2.86 GPa, three times higher than those for Al materials produced through electrodeposition from a well-known ionic liquid bath or through severe plastic deformation. Additionally, the void-free Al deposits had a <100> preferential crystal orientation, which accounted for better resistance to free corrosion and pitting corrosion. Discussions about the compact microstructure and <100> crystal orientation of deposits obtained only from the $x = 0.4$ concentrated electrolyte are also presented.

Keywords: aluminum electrodeposition; concentrated electrolyte; diglyme; hardness; corrosion

1. INTRODUCTION

Concentrated electrolytes, which have been viewed as key materials for next-generation batteries and plating, attract considerable attention in materials science.[1-5] Not only the electrolyte properties but also the electrodeposition behaviors are attractive in terms of safety, cost, and functionalities. Concentrated electrolytes contain less free solvents, giving decreased activities of solvents or less volatilities and less reactivities: thus, the better thermal stabilities and better (electro)chemical stabilities contribute to the safety. The properties of metal electrodeposits are also of interest because compact and smooth deposits can be obtained from the concentrated electrolytes,[4-6] which are useful as negative electrode materials and plating materials. The electrodeposition behaviors differ from those of non-concentrated electrolytes due to the different physicochemical properties of the electrolytes.

Aluminum (Al) is a naturally abundant element, and metallic Al has various functional properties such as lightweight, corrosion resistance, low redox potential (–1.68 V *vs.* SHE), and large theoretical capacity (2,979 Ah kg^{-1} or 8,042 Ah dm^{-3}). Al has been utilized as a structural and corrosion protection material,[7] and recently considered as an electrode material for secondary ion battery.[8-11] It is well known that Al can be electrodeposited from many kinds of nonaqueous electrolytes, which can be classified as concentrated and non-concentrated electrolytes. The concentrated electrolytes include high temperature molten salts,[12] room temperature molten salts or ionic liquids (ILs),[13-17] and deep eutectic solvents or solvate ionic liquids.[18-23] The compact and smooth Al deposits can be obtained from these concentrated electrolytes,

therefore, they have been used as a corrosion-resistant layer deposited on the carbon steel and magnesium alloys.[15-17] The non-concentrated ones employ the nonpolar/less-polar solvents such as ethers and aromatic hydrocarbons.[24-26] And recently, a polyether i.e., diglyme (G2) with a high boiling point (162 °C) and chelating ability was employed for Al electrodeposition at room temperature.[27-33] G2 is less toxic and volatile than conventional ethers, such as diethyl ether and tetrahydrofuran, or aromatic hydrocarbons.[34] Since G2 is industrially produced as a raw material of surfactants, the G2-based electrolyte should be cost-effective. In addition, compared to the $AlCl_3$-containing molten salts or ionic liquids,[13-17] the G2-based electrolytes have lower molar ratio of $AlCl_3$ which makes them less Lewis acidic and thus less corrosive. However, the non-concentrated $AlCl_3$–G2 bath with an $AlCl_3$/G2 molar ratio x = 0.2 can only produce the loose and rough Al deposits under a potentiostatic electrodeposition,[27-30] which may have an adverse effect on the mechanical properties and corrosion resistance.

In concentrated electrolytes, most solvent molecules will coordinate with metal ions. It will reduce the amount of free solvent molecules and its activity, which improve the electrolyte properties.[1,2] Furthermore, it has been reported that the use of concentrated *aqueous* electrolytes can decrease the thickness of diffusion layer, which contributes to the smooth deposits.[4] To examine the effect of concentration in *nonaqueous* electrolytes on the electrodeposition behaviors, a concentrated $AlCl_3$–G2 bath are investigated in this study. Smooth and void-free Al deposits with improved mechanical/corrosion-resistant properties are successfully obtained, and discussions about the compact microstructure and the growth mode are also presented.

2. EXPERIMENTAL SECTION

2.1 Chemicals and electrolyte preparation. G2 was purchased from Kanto Chemical Co. and high purity anhydrous $AlCl_3$ was kindly supplied by the Nippon Light Metal Co. The G2 and $AlCl_3$ were mixed in a glovebox with O_2 content below 1.0 ppm. Figure S1 (Supporting Information) shows photographs of $AlCl_3$–G2 solutions at about 25 °C. A clear and light yellow color solution was obtained in the case of x = 0.1, 0.2, and 0.4. The $AlCl_3$–G2 solution got to the saturation between x = 0.4 and 0.45, and it became a solid at x = 0.67. Although the $AlCl_3$–G2 solution with x = 0.67 was a liquid at 60 °C, its melting point increased with time due to the evaporation of G2. Therefore, the x = 0.1, 0.2, and 0.4 were used, corresponding to the $AlCl_3$ concentration of 0.68, 1.33, and 2.5 mol dm^{-3}. In this work, the $AlCl_3$–G2 solution with x = 0.4 is regarded as a concentrated solution at room temperature.

2.2 Bath properties. Viscosities of the electrolytes were measured using an electromagnetic spinning viscometer (EMS-1000). Samples were sealed in glass tubes filled with argon (Ar). Based on the electrochemical impedance spectroscopy, the conductivities were measured using a self-made two-stainless steel-electrode cell, and the cell constant was calibrated with 0.1 mol dm^{-3} KCl aqueous solution (1.285 S m^{-1} at 25 °C).[35] ^{27}Al NMR spectra were obtained (200 scans, acquisition time 1.5 s) at 25 °C using nuclear magnetic resonance spectrometer (600 MHz, JNM-ECA 600), referenced to DMSO-d_6 (99.9 at% D, Sigma-Aldrich).

2.3 Electrochemical measurements for electrolytes and electrodeposition.

Cyclic voltammogram and electrodeposition were conducted using Biologic VSP–300 in a standard three-electrode cell. The electrochemical cells used in this study were glass-beaker cells (20 cm^3) and gold-plated clips to avoid possible corrosion by the electrolyte. A copper (Cu) sheet (99.96%, Nilaco Co.) was used as a working electrode, while two aluminum sheets (99.99%, Nilaco Co.) as a counter electrode and a quasi-reference electrode (QRE). The Cu substrate was cleaned by acetic acid for 30 min to remove copper oxides effectively,[36] and then washed by ultrasonication in acetone and ethanol for 20 min, respectively. To obtain Al electrodeposits with high throwing-power and to minimize the effect of chlorine impurity on the hardness of Al deposits, we performed a long-term pre-electrodeposition process, *i.e.* a potentiostatic method at –1.0 V vs. Al QRE for 10 d, after which the chlorine content in Al deposits has been reduced to a stable value of about 0.2 at%. The potentiostatic electrodeposition at –1.0 V vs. Al QRE was carried out for Al electrodeposition. After the electrodeposition, the samples were rinsed into pure G2, acetone and ethanol successively to remove the remaining electrolyte, and then stored in glove box to minimize spontaneous oxidation.

2.4 Microstructural characterization of electrodeposits. X-ray diffraction (XRD, Rigaku RINT2200) measurements were performed at a scan rate of 0.3° min^{-1}. Surface and cross-sectional morphologies of deposits were characterized by scanning electron microscopy (SEM, Keyence VE-7800) and transmission electron microscope (TEM, JEM-2100F). The deposits and substrate were separated during ultrasonic cleaning, and the deposits were collected for XRD measurement and SEM cross-sectional observation. The samples for TEM observation were prepared by the focused

ion beam system (FIB, JEOL JFIB-2300), and then placed on copper mesh.

2.5 Nanoindentation measurements. The mechanical properties of the Al deposits were characterized using a Hysitron TI 950 Triboindenter instrument equipped with a Berkovich indenter. The load and displacement resolutions were 1 nN and 0.04 nm, respectively. The nanoindentation was tested at a maximum of 500 μN with a holding time of 5 s. The loading and unloading rates were all 0.1 mN s^{-1}. The separated samples were polished with the colloidal silica (0.08 μm) before measurement. The penetration of the indenter is less than 10% of the thickness of the sample, hence, the influence of the substrate on the results can be neglected. To determine the hardness and elastic modulus of the deposits, the initial part of unloading curves was fitted by the Oliver-Pharr method.[37] For all samples, 20 measurements were repeated. In-situ scanning probe microscopy (SPM) imaging (1 μm × 1 μm area) was also conducted with a scan rate of 1 Hz, scan size of 1 μm × 1 μm and contact force of 2.0 μN.

2.6 Corrosion tests. The electrochemical corrosion experiments were carried out in a 3.5 wt% NaCl aqueous solution at room temperature. Platinum and saturated calomel electrodes (SCE) were used as the counter electrode and reference electrode, respectively. The separated Al deposits were polished with colloidal silica (0.08 μm). All samples were immersed in 3.5 wt% NaCl solution for 5 h until a stable open-circuit voltage. The electrochemical impedance spectroscopy (EIS) was detected in the frequency range of 100 kHz–10 mHz with a sinusoidal perturbation of ±10 mV. The cyclic polarization curves started at 0.1 V more negative than the OCV and were

recorded at a scan rate of 1 mV s^{-1}. The sweep direction was reversed at a current density of 1 mA cm^{-2}.

3. RESULTS

3.1 Bath composition and properties. Figure 1 shows the ^{27}Al NMR for the x = 0.4 with 2.5 mol dm^{-3} $AlCl_3$. The spectra consisted were assigned as $AlCl_4^-$ (105.8 ppm, Figure 1(a)), $AlCl_3$·G2 (61.8 ppm, Figure 1(b)) and $[AlCl_2(G2)_2]^+$ (27.3 ppm, Figure 1(b)) according to Nöth et al., who had measured $AlCl_3$–G2 electrolytes below 1.7 mol dm^{-3} $AlCl_3$.[38] It should be noted that the $AlCl_3$·G2 was only detected in the $AlCl_3$–G2 with $AlCl_3$ lower than 0.21 mol dm^{-3},[38] probably due to the resolution at that time. The molar ratio of the dissolved species was analyzed using their integral areas. As a result, $AlCl_4^-$ anion and $[AlCl_2(G2)_2]^+$ cation were almost equimolar, and the $AlCl_3$·G2/$[AlCl_2(G2)_2]^+$ was as low as 0.03. This may be consistent with the fact that x = 0.4 is near saturation. For lower $AlCl_3$ concentration, the molar ratio $AlCl_3$·G2/$[AlCl_2(G2)_2]^+$ increased to 0.14 (x = 0.2) and 0.27 (x = 0.1). Therefore, the equilibrium occurred in the $AlCl_3$–G2 electrolytes can be expressed as the following equations.

$$2AlCl_3 + 2G2 \rightleftharpoons 2AlCl_3 \cdot G2 \quad (1)$$

$$2AlCl_3 \cdot G2 \rightleftharpoons [AlCl_2(G2)_2]^+ + AlCl_4^- \quad (2)$$

This equilibrium was also found in the solvate ILs when the $AlCl_3$/solvent molar ratio was not greater than 1.[39] It may be notable that in Equation (2), the x = 0.4 had an

equilibrium constant K of 3.0, while it was decreased to 1.7 and 1.1 for $x = 0.2$ and 0.1, respectively. We would also like to note that the $x = 0.2$ system, which definitely contain free G2, were categorized into ILs in some literatures.[23]

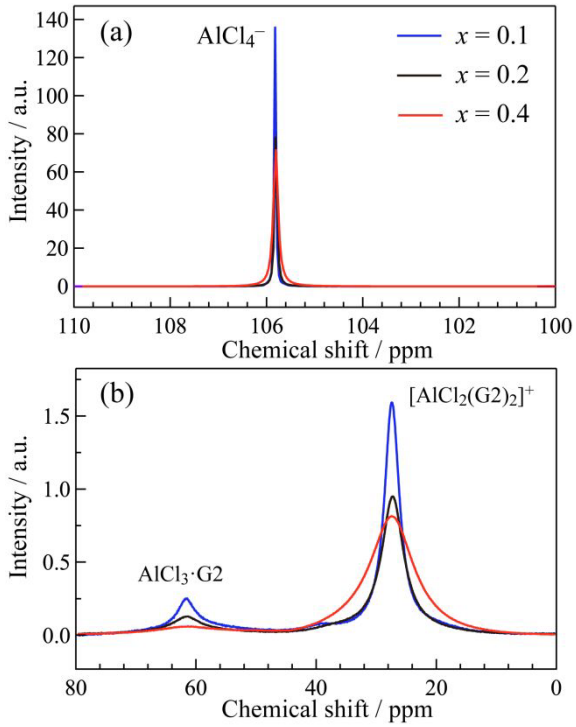

Figure 1. ^{27}Al NMR spectra of $x = 0.1$, 0.2 and 0.4 in a range of (a) 100–110 ppm and (b) 0–80 ppm.

Figure 2 shows the ^{1}H NMR spectra of the $AlCl_3$–G2 electrolytes. The assignments of ^{1}H NMR signals are shown in the inset of Figure 2. By dissolving the $AlCl_3$ into G2, the signals became broader, which was also found in ^{27}Al NMR spectra (Figure 1). The broadening of the signals was due to the increase in viscosity.[40] In addition, the ^{1}H NMR spectra for $x = 0.4$ shifted to a higher magnetic field than that in pure G2 and in $x = 0.1$ and 0.2. The free G2 and the G2 in the Al^{3+}–Cl–G2 complex cannot be distinguished by ^{1}H NMR due to a fast ligand exchange rate in $AlCl_3$–G2 electrolytes.[1] The lifetime

(τ) of the free G2 in $AlCl_3$–G2 electrolytes can be estimated by the following equation:[1]

$$\tau = \frac{2\,(W - W_0)}{\pi f (\delta - \delta_0)^2} \quad (3)$$

where the W_0 and δ_0 are the full width at half-maximum and the chemical shift of the NMR signal of the end methyl proton of pure G2, respectively. The W and δ are the full width at half-maximum and the chemical shift of end methyl proton of Al^{3+}–Cl–G2 complex, respectively. The f is the frequency (600 MHz) of NMR spectrometer. The estimated τ value was 1.3×10^{-4} s for $x = 0.4$. As the x decreased to 0.2 and 0.1, the corresponding τ increased to 1.7×10^{-4} s and 2.1×10^{-4} s, respectively. These τ values are the same order of magnitude as those in Li^+–glyme solvate ILs.[1]

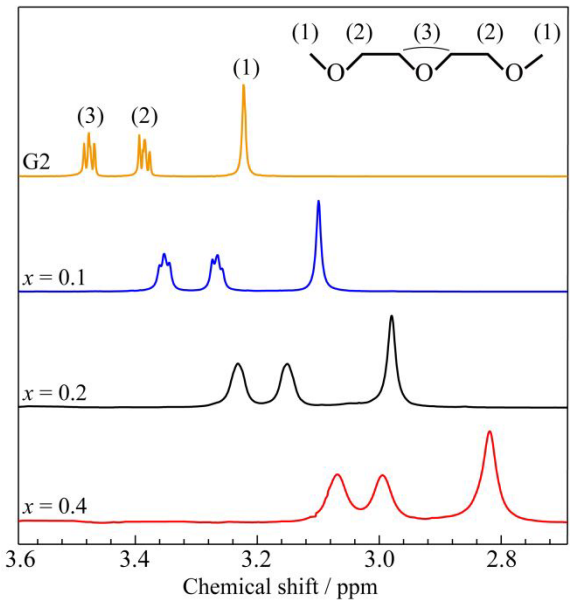

Figure 2. ^{1}H NMR spectra of $x = 0$, 0.1, 0.2 and 0.4 in a range of 2.7–3.6 ppm.

The viscosity (η) and ionic conductivity (σ_c) as a function of temperature for the $AlCl_3$–G2 electrolytes are shown in Figure S2 (Supporting Information). The linear relationship between ln η or ln σ_c and T^{-1} are observed in Figure S2(c) and (d), obeying the Arrhenius law. The Walden plots, i.e. the plots of molar conductivity (Λ_{imp}) versus

fluidity (η^{-1}), are frequently used to evaluate how electrolytes are relatively conductive compared to ideal KCl aqueous solution.[41-43] Figure 3 shows the Walden plots of the $AlCl_3$–G2 electrolytes together with the ideal KCl aqueous solution. The ratio of $\Lambda_{imp}/\Lambda_{ideal}$ can be obtained from the difference in the vertical axis, i.e., $\log(\Lambda_{imp}/\Lambda_{ideal})$, giving $\Lambda_{imp}/\Lambda_{ideal} = 0.40$ at all temperatures for $x = 0.4$. Before calibration, namely without considering the neutral $AlCl_3$·G2, it seemed that the concentrated electrolyte had a prominent "ionicity" than those of $x = 0.2$ and 0.1. However, it should be noted that the ^{27}Al NMR signal arising from $AlCl_3$·G2 was clear in $x = 0.1$ and 0.2 (Figure 1(b)). The Λ_{imp} was calibrated based on the ^{27}Al NMR observation. The calibrated $\Lambda_{imp}/\Lambda_{ideal}$, namely just considering the ionic complex in $x = 0.1$ and 0.2 electrolytes, was almost same as that for $x = 0.4$. Therefore, the total correlation of cation-cation, cation-anion, anion-anion interactions seems to be similar for x in this study.

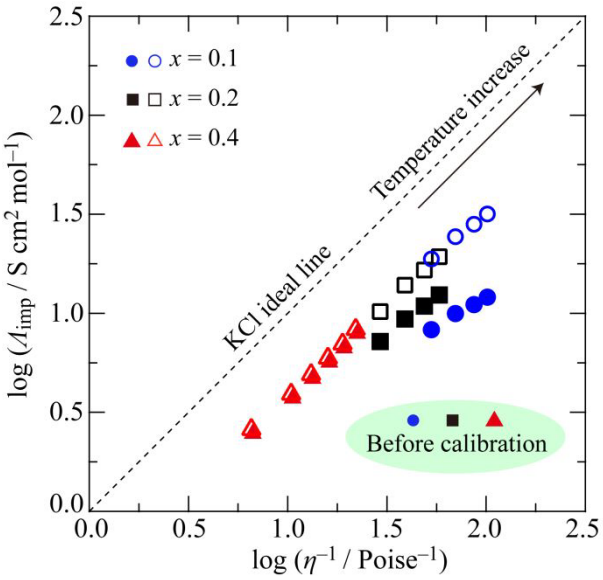

Figure 3. Walden plots for $x = 0.1$, 0.2 and 0.4, where 1 Poise = 100 mPa s.

3.2 Microstructure and crystal orientation of deposits. A set of typical cyclic

voltammograms of the $AlCl_3$–G2 electrolytes is shown in Figure S3 (Supporting Information). The clear cathodic current was observed at an electrode potential lower than –0.35 vs. Al QRE. The difference in the current densities among x = 0.1, 0.2 and 0.4 is correlated with the different ionic conductivities of electrolytes shown in Figure S2(b) (Supporting Information). The highest ionic conductivity is obtained for x = 0.2, while those for 0.1 and 0.4 are similar. Accordingly, the current density of CVs is the highest for x = 0.2, while those for 0.1 and 0.4 are similar. The potentiostatic electrodeposition at –1.0 V vs. Al QRE has been conducted on Cu for 6 h, and the current density was almost constant at 10, 21 and 13 mA cm^{-2} for x = 0.1, 0.2 and 0.4. After the potentiostatic electrodeposition, the Cu substrates were covered by deposits (Figure 4(a), (d), and (g)) and the XRD results revealed that the deposits were pure Al with no significant impurities (Figure 5(a)). In the concentrated $AlCl_3$–G2 electrolyte (x = 0.4), Al deposits had a compact and smooth morphology (Figure 4(h)) showing a metallic luster (Figure 4(g)), and there was no visible void on the cross-sectional view (Figure 4(i)). Even by changing electrodeposition time (1 h, 6 h and 12 h), the Al deposits exhibited a similar surface morphology. We also did the electrodeposition at a more negative potential (–1.5 V vs. Al QRE), namely at a higher current density. However, it did not further improve the roughness of the deposits. Notably, a further enhancement in concentration to x = 0.43 also produced a similar Al deposits (–1.0 V vs. Al QRE, 1 h; see Figure S4, Supporting Information); however, white precipitates appeared in the x = 0.43 electrolyte during a long-term electrodeposition. In contrast, the Al deposits obtained from the dilute electrolytes, including x = 0.1 and 0.2, had a

flake-like surface morphology (Figure 4(b) and (e)), resulting in a rough surface with a black appearance (Figure 4(a) and (d)). And many micro-voids were found on the cross-sectional view (Figure 4(c) and (f)).

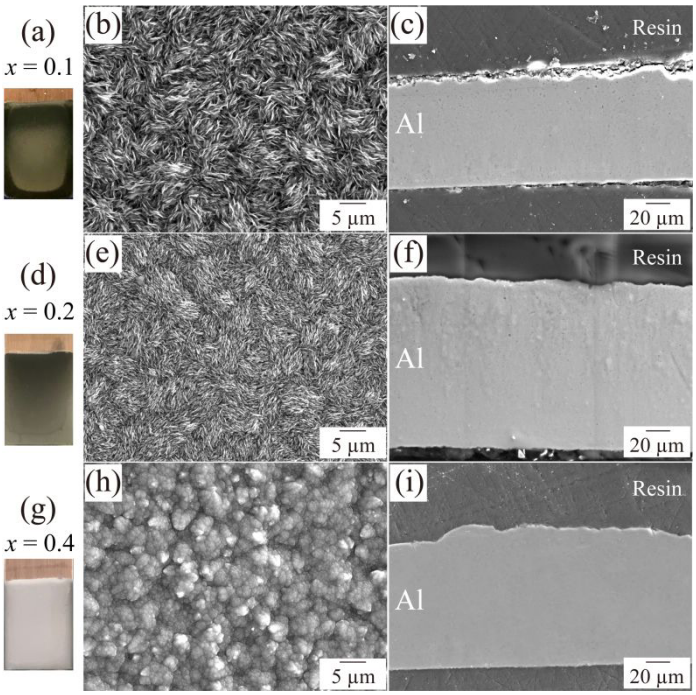

Figure 4. Photographs and SEM images of Al deposits obtained potentiostatically at –1.0 V vs. Al QRE from the (a)–(c) $x = 0.1$, (d)–(f) $x = 0.2$ and (g)–(i) $x = 0.4$.

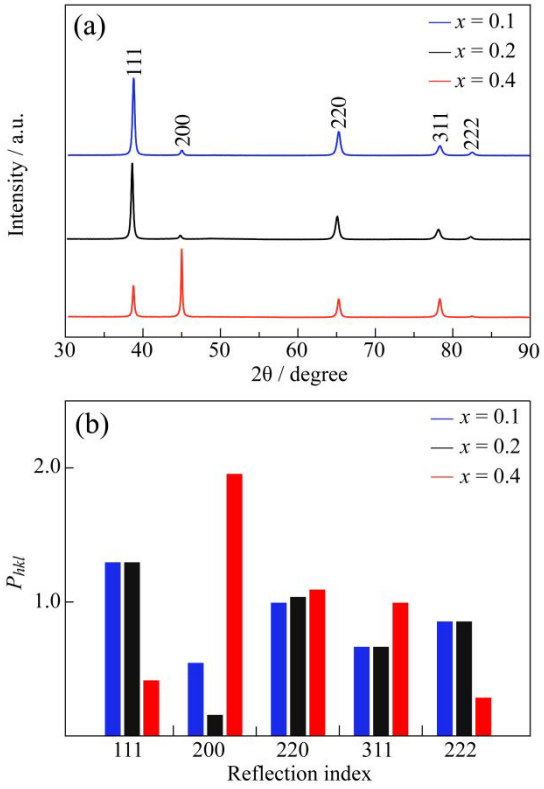

Figure 5. (a) XRD of the Al deposits obtained potentiostatically at –1.0 V vs. Al QRE from x = 0.1, 0.2 and 0.4. (b) presented the normalized peak intensity P_{hkl} of XRD.

To explore the causes of voids in Al deposits obtained from dilute electrolytes, a sample with a thickness about 5 μm was prepared by potentiostatic deposition at –1.0 V vs. Al QRE for about 15 min in x = 0.2. Figure 6(a)-(c) shows the TEM dark-field images of the cross-section of the deposits. The flake-like structure only existed in the upper layer (above the yellow line in Figure 6(b)), i.e. the interface between deposits and electrolytes. The flake-like Al deposits grew parallelly (marked by yellow arrows) or at a certain angle (marked by red arrows). Thus, the voids marked by yellow and red colors in Figure 6(c) were enclosed by the adjacent Al flakes, where the yellow and red voids were from the parallel and nonparallel flakes, respectively. The reduced Al particles were easily captured by the tip of flake-like Al deposits and shielded to

aggregate on the hollow position, therefore, this kind of flake-like structure still appeared on the surface of deposits even after a long-time electrodeposition (Figure 6(b)). Therefore, the micro-voids in Al deposits was related to the flake-like structure, and the same logic can be applied to the Al deposits obtained from $x = 0.1$ (Figure S5, Supporting Information). In contrast, the concentrated $AlCl_3$–G2 electrolyte produced a compact and smooth Al deposit (Figure 6(d)) due to a spherical microstructure shown in Figure 4(h).

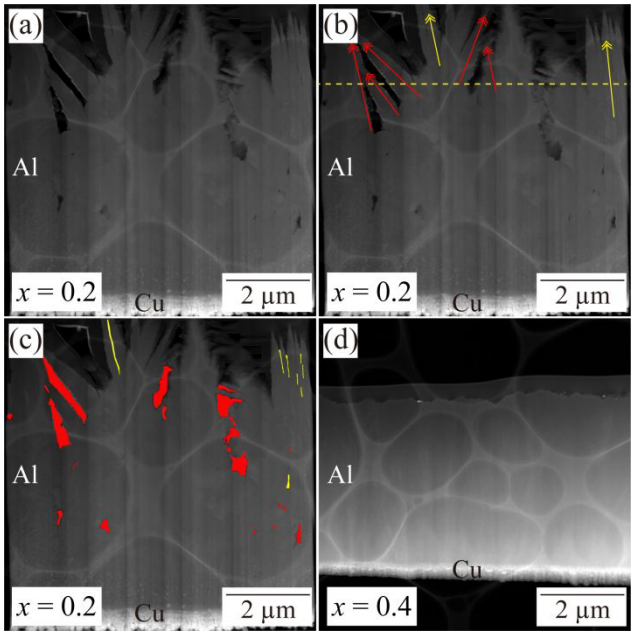

Figure 6. The cross-sectional TEM dark-field images of Al deposits obtained potentiostatically at –1.0 V from the (a)–(c) $x = 0.2$ and (d) $x = 0.4$. The flake-like structure and micro-voids in (a) are emphasized in (b) and (c), respectively.

The crystallographic orientation of Al deposits shown in Figure 5(a) can be evaluated by the normalized integrated intensity P_{hkl} according to the following equation:[14]

$$P_{hkl} = \frac{I_{hkl} / \sum I_{hkl}}{I°_{hkl} / \sum I°_{hkl}} \quad (4)$$

where I_{hkl} and $I°_{hkl}$ are the peak intensities for *hkl* reflection of our Al deposits and of the standard PDF card data (No. 00-004-0787), respectively. The Al deposit with a strong orientation of <100> was obtained in the concentrated electrolyte $x = 0.4$ (Figure 5(b)). However, as the x decreased, the Al deposits presented a mild orientation of <111> and the <100> reflection had the least P_{hkl} for $x = 0.1$ and 0.2.

An alternative electrochemical technique, namely galvanostatic electrodeposition at 15 mA cm^{-2} for 6 h, was also performed to prepare the Al deposits. Each potential was almost constant at about –1.4 V, –0.8 V and –1.1 V vs. Al QRE for $x = 0.1$, 0.2 and 0.4. Similar to the potentiostatic technique (Figure 4), the Al deposits obtained by galvanostatic electrodeposition also presented flake-like and spherical surface morphologies for the dilute and concentrated $AlCl_3$–G2 electrolytes, respectively (Figure S6, Supporting Information). Besides, compared to the potentiostatic technique (Figure 5), the galvanostatic electrodeposition made little difference to the crystallographic orientation of Al deposits (Figure S7, Supporting Information). In this study, only Al deposits obtained by the potentiostatic electrodeposition were used for the following nanoindentation and corrosion tests.

3.3 Mechanical properties. There have been several studies using micro-Vickers and nanoindentation tests to explore the mechanical properties of Al deposits. The Al deposits obtained from $AlCl_3$–sulfone baths show a micro-hardness of 0.24 GPa–1.7 GPa,[44-46] while those obtained from $AlCl_3$–G2 bath with $x = 0.2$ show 1.62 GPa.[30] However, the micro-hardness and nano-hardness cannot be compared directly because

of the different indentation size.[47] Moreover, both nano-hardness and elastic modulus are available from the nanoindentation tests. For instance, in the $AlCl_3$–1-ethyl-3-methylimidazolium chloride ([EMIm]Cl) ILs baths, the Al deposits with a crystallite size of 1 μm and 2 μm have ever been obtained.[17, 48] They correspond to a nano-hardness of 0.9 GPa and 0.71 GPa, respectively. Meanwhile, the corresponding elastic modulus is 65.2 GPa and 44.9 GPa, respectively.

Figure 7 shows the load-displacement curves of Al obtained from $AlCl_3$–G2 electrolytes. The Al deposits obtained in the concentrated $AlCl_3$–G2 electrolyte had a nano-hardness and elastic modulus of 2.86±0.02 GPa and 60.86±0.52 GPa, respectively. The nano-hardness (elastic modulus) of the Al deposits was 2.17±0.03 GPa (62.44±1.19 GPa) for x = 0.2 and 2.10±0.02 GPa (57.76±1.45 GPa) for x = 0.1. Figure 8 shows the SPM images (Figure 8(a)-(f)) and cross-sectional profiles (Figure 8(g)-(i)) of the indents in Al deposits after the nanoindentation test. The combination of SPM images (Figure 8(c) and (f)) and cross-sectional profile (Figure 8(i)) revealed that Al deposits from the concentrated $AlCl_3$–G2 electrolyte exhibited clear pile-up around the edges of the contact. However, the pile-up was slight for x = 0.2 as shown in Figure 8(h) and even disappeared for x = 0.1 as shown in Figure 8(g).

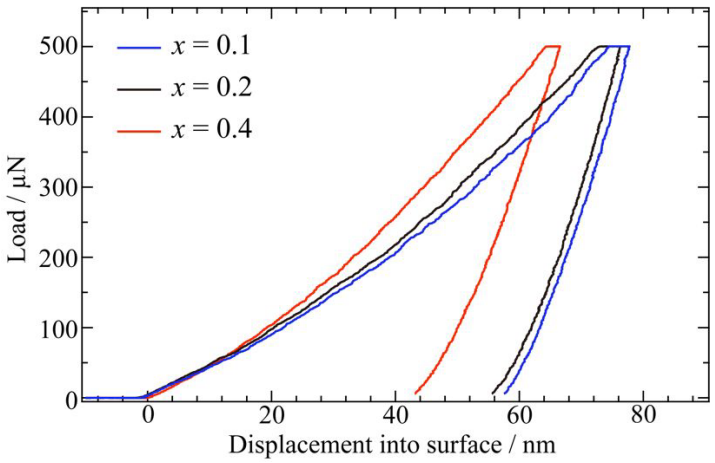

Figure 7. Load-displacement curves of the Al deposits with different *x*.

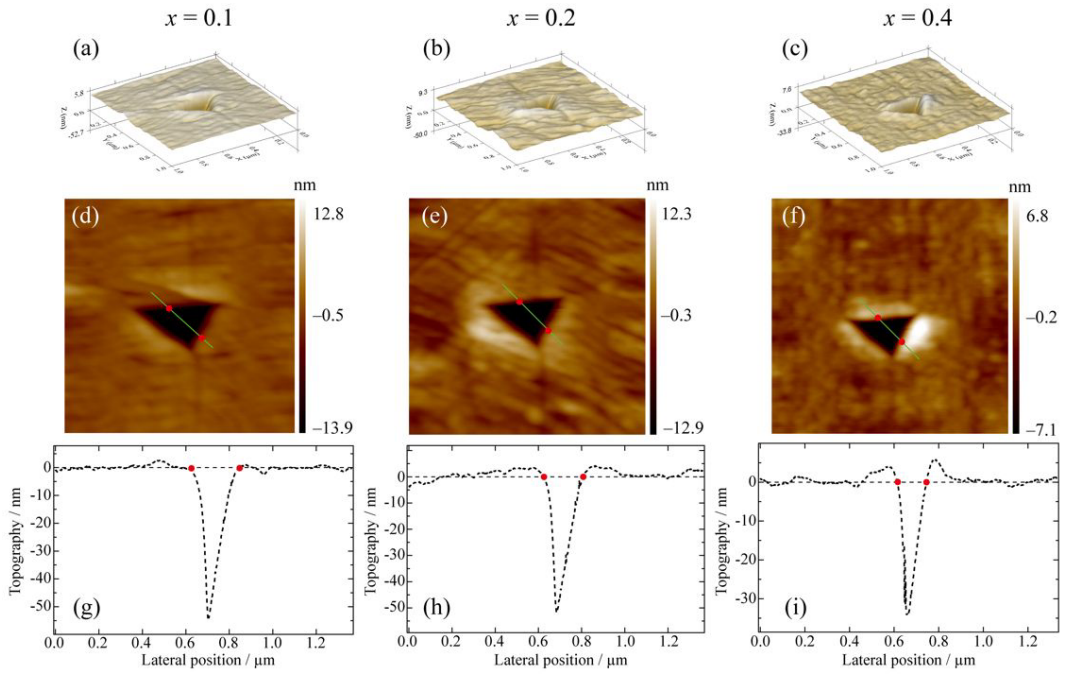

Figure 8. (a)–(f) In-situ scanning probe microscopy images and (g)–(i) the corresponding cross-sectional traces of Al deposits with different *x*: (a,d,g) *x* = 0.1, (b,e,h) *x* = 0.2 and (e,f,i) *x* = 0.4.

It is worth mentioning that impurities (e.g. S and Cl) absorbed on cathode during electrodeposition, and the impurities in deposits with content higher than 1.0 at% lead

to an increased hardness.[44] The impurity contents were checked by analysis of TEM–EDS from the TEM samples shown in Figure 6 and Figure S5 (Supporting Information). The Cl content in Al deposits for x = 0.1, 0.2 and 0.4 was 0.21 at%, 0.27 at% and 0.22 at%. The Al deposits obtained from $AlCl_3$–G2 electrolytes had a Cl content less than 0.3 at%, therefore, the effect of Cl impurity on the hardness of Al can be excluded. Likewise, the other tiny amount of impurities including O and C should affect less on the hardness of Al deposits.

3.4 Corrosion behaviors. The Nyquist plots for Al deposits are shown in Figure 9, which were all associated with a smaller arc-like capacitive loop at a higher frequency and a larger capacitive loop at a lower frequency. The smaller capacitive loop is related to the process of charge transfer at the electrolyte/surface oxide film/Al interfaces and its diameter could present the inhibitive action of specimen.[49] The diameter increased as x increased. These Nyquist plots can be fitted by an equivalent electrical circuit model $R_s\,(C_f\,(R_f(C_{dl}\,R_{ct}))$ (see inset of Figure 9) with the smallest Chi-square deviations (χ^2) value within 0.01%. The fitted parameters are presented in Table S1 (Supporting Information). The equivalent electrical circuit comprised solution resistance (R_s), surface oxide film resistance (R_f), oxide film capacitance (C_f), double layer phase element capacitance (C_{dl}) and charge transfer resistance (R_{ct}). In addition, the R_p ($R_p = R_f + R_{ct}$) refers to the polarization resistance, which is inversely proportional to the corrosion rate.[49] As shown in Table S1 (Supporting Information), the R_p value (9.4 kΩ cm^2) was the lowest for x = 0.1, followed by R_p (20.4 kΩ cm^2) for x = 0.2, and the highest for x = 0.4 (25.1 kΩ cm^2). The standard errors of R_p value was less than 3%.

The n_f and n_{dl} are the empirical exponents of the C_f and C_{dl}, respectively. The $0.5 < n < 1$ is associated to an inhomogeneous nature of the electrode surface, while $n = 1$ corresponds to a purely capacitor.[50] Figure S8 (Supporting Information) shows the Bode plots for the Al deposits in 3.5 wt% NaCl solution. The magnitude plots (Figure S8(a), Supporting Information) show that the absolute impedance value increases as x increases. It is also observed that the maximum phase angle (θ_{max}) at a medium frequency increases as x increases (Figure S8(b), Supporting Information). In addition, the Bode phase angle plot extends over the widest range of frequencies for Al deposits obtained in $x = 0.4$. A lager θ_{max} and broader phase angle peak in Bode plots imply that the Al deposits has a better barrier effect against corrosive ingress.[49]

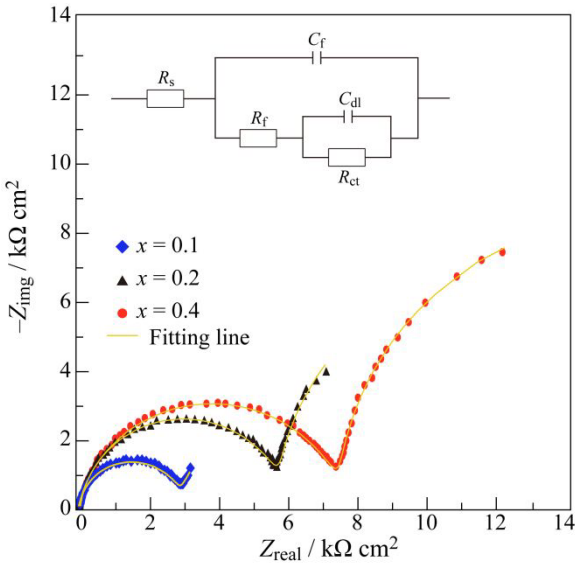

Figure 9. Nyquist plots of the Al deposits obtained from $x = 0.1$, 0.2 and 0.4 in 3.5 wt% NaCl aqueous solution.

Figure 10 shows the cyclic polarization curves for the Al deposits obtained from different electrolytes. Table 1 lists the characteristic parameters in Figure 10. The free

corrosion potential (E_{corr}) was the highest for $x = 0.4$, followed by $x = 0.2$, and lowest for $x = 0.1$. The corrosion current density (i_{corr}) exhibited an opposite trend. Furthermore, for each sample a wide passive region was observed from E_{corr} to a pitting potential (E_{pit}). After that, a steep increase of anodic current density indicates that pits nucleate and grow upon the E_{pit}. The E_{pit} shifted to a more positive potential from $x = 0.1$ and 0.2 to 0.4. Higher E_{corr} and E_{pit} prove for $x = 0.4$ a better ability to prevent free and pit corrosion in chloride-containing solution. These results were in good agreement with the results indicated in EIS spectra (Figure 9). Afterward, the scan direction was reversed at a predetermined threshold of current density 0.5 mA cm^{-2}. A current hysteresis loop was formed as the reversed scan intersecting with the anodic scan. The intersection pointed by dots in Figure 10 is the protective potential (E_{prot}) and a higher potential is denoted as the pitting transition potential (E_{ptp}). E_{ptp} corresponds to a re-passivation of shallow pits. Therefore, its appearance in all Al deposits means that the deeper pits are formed during scan upon E_{pit} and they need a more negative potential E_{ptp} to be re-passivated.[51-53] E_{ptp} is more positive for $x = 0.4$ than that for $x = 0.1$ and 0.2, which indicates an easier re-passivation of shallow pits for $x = 0.4$.

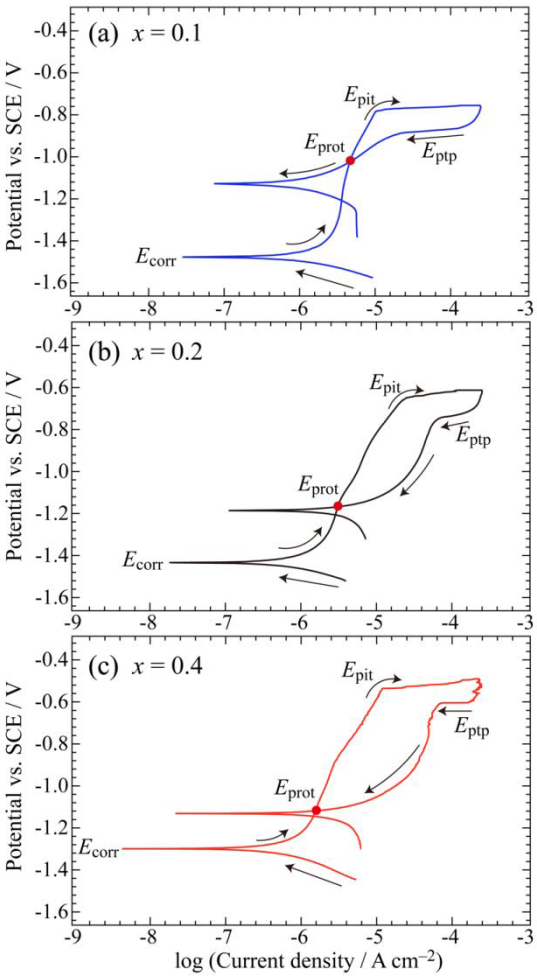

Figure 10. Cyclic polarization curves of Al deposits obtained in 3.5 wt% NaCl aqueous solution for (a) $x = 0.1$, (b) $x = 0.2$ and (c) $x = 0.4$.

Table 1. Characteristic parameters obtained from the corrosion tests.

Molar ratio x	E_{corr} / V	i_{corr} / μA cm^{-2}	E_{pit} / V	E_{ptp} / V	E_{prot} / V
0.1	–1.48	0.62	–0.78	–0.88	–1.20
0.2	–1.43	0.39	–0.64	–0.73	–1.16
0.4	–1.30	0.24	–0.53	–0.60	–1.16

4. DISCUSSION

Compared to the aforementioned Al deposits obtained from $AlCl_3$–[EMIm]Cl ILs,[17, 48] the nano-hardness of Al deposits have been significantly improved for the concentrated $AlCl_3$–G2 electrolyte. In addition, as for the bulk Al with a crystallite size of 1.2–1.5 μm produced through severe plastic deformation, the nano-hardness and elastic modulus are approximately 0.85 GPa and 72 GPa, respectively.[47] The crystallite size of the present Al deposits is about 15 nm observed by dark-field TEM and high-resolution transmission electron microscopy (HRTEM) images (Figure S9, Supporting Information). Using the $AlCl_3$–[EMIm]Cl ILs, Rafailović et al. reported an Al deposits with high density of twins on the Ag substrate, which contributed to the improvement of hardness.[48] In our work, however, the twins in Al deposits were not observed. Therefore, the dramatically higher nano-hardness of the deposited Al should be attributed to a significant grain size refinement.[54] However, the present nanocrystalline Al deposits has a decreased elastic modulus, which is a common phenomenon for nanosized materials.[55]

The yield stress (σ_y) of the Al deposits can be estimated from the Tabor's relation $H = C\sigma_y$, where H is the indentation hardness and C has a value of approximately 4 for Al.[56] The σ_y is calculated to be 715 MPa for the Al deposits from $x = 0.4$. The classical Hall–Petch relationship has been well established for bulk Al (purity 99.99 wt% and 99 wt%) with crystallite size (d) over 0.22 μm (Figure S10, Supporting Information).[57-58] In Figure S10, although the impurity elements are different between the bulk Al (Si, Fe, Cu, etc.) and the electrodeposited Al (Cl), the yield stress of Al deposits deviates

from the extrapolated Hall–Petch plot for bulk Al, indicating an inverse Hall–Petch behavior. Such behavior is also observed in another nanograined metals with grain size smaller than 30 nm because of a grain boundary (GB)-mediated process.[55, 59]

As shown in Figure 8(i), the appearance of pile-up around an indent indicates that plastic deformation is localized (or confined) within a small volume due to the poor strain hardening ability.[60] Therefore, although the Al deposits from $x = 0.4$ has a higher nano-hardness, it has a worse strain hardening ability. In fact, this phenomenon is very common in a bulk metallic material, namely the ultra-refinement of grain size usually causes higher strength but poor strain hardening ability.[61] It is noteworthy that the pile-up was slight for $x = 0.2$ (Figure 8(h)) and even disappeared for $x = 0.1$ (Figure 8(g)), which indicate that the mechanical properties of Al deposits with micro-voids deviate from that of compactly bulk Al. It has been reported that the micro-voids degrade the hardness of metallic films and the hardness of Al shows dependence on crystal orientation, where the <100> orientation exhibits a maximum hardness.[62-63] Therefore, the nano-hardness of Al deposits obtained in $x = 0.4$ is higher than that obtained in dilute electrolytes, which is due to a compact microstructure (Figure 4(g)-(i)) and strong <100> orientation (Figure 5).

A significant improvement in corrosion resistance is also achieved for the concentrated $AlCl_3$–G2 electrolyte. A strong dependence of pitting behavior on the crystal orientation of Al has ever been reported.[52] It is believed that the difficulty of pits nucleation in aqueous NaCl solution increases in this order (111) < (110) < (100).[64] In concentrated $AlCl_3$–G2 electrolyte, the (100) crystal face of Al deposits has priority

over (111), while in x = 0.1 and 0.2 the preferential crystal face is (111) (Figure 5(b)). Therefore, the x = 0.4 sample has the most positive E_{pit} and higher resistance to pitting corrosion (Figure 10), not only due to the void-free nature different from the x = 0.1 and 0.2 samples (Figure 4).

As discussed above, it is obvious that the mechanical properties and corrosion behaviors of Al deposits largely depend on the microstructure and crystal orientation of deposits. Therefore, the further discussion about the compact microstructure and <100> crystal orientation of deposits is essential. In general, to obtain dense and smooth metal deposits, decrease in the thickness of the diffusion layer is important. One method is to increase the concentration of electrochemically active species in bulk and/or the vicinity of electrode, by simply using concentrated electrolytes and/or using pulse electrodeposition.[6, 65] Another method is to realize "mild depletion" of the electrochemically active species near the electrode/electrolyte interface: examples include pulse electrodeposition with triangular-wave in the x = 0.2 bath or small diffusion coefficients due to large viscosities in a highly concentrated aqueous bath.[4, 29] By using the concentrated $AlCl_3$–G2 electrolyte, in contrast, the smooth and dense Al deposits can be obtained even by potentiostatic/galvanostatic techniques or without using pulse techniques. For x = 0.1 and 0.4, in particular, the $AlCl_3$–G2 electrolytes have a similar conductivity but one order of magnitude different viscosities (Figure S2(a) and (b), Supporting Information). Therefore, we consider that the thickness of the diffusion layer in the concentrated electrolyte is smaller than that in x = 0.1 and 0.2, resulting in the compact microstructure with spherical particles.

The absorption of neutral organic molecules on cathode during electrodeposition will also influence the microstructure of deposits.[66] The $AlCl_3$·G2 complex and free G2 are the principal neutral organic molecules in $AlCl_3$–G2 electrolyte. As for the concentrated $AlCl_3$–G2 electrolyte, the ^{27}Al NMR spectra shown in Figure 1 reflect that the content of the neutral $AlCl_3$·G2 has been decreased to a very low level, and the Walden plots shown in Figure 3 reveal that almost the whole $AlCl_3$ asymmetrically split to generate ionic complex in the concentrated $AlCl_3$–G2 electrolyte. In addition, the lifetime (τ) of free G2 in the concentrated $AlCl_3$–G2 electrolyte is smaller than that in x = 0.1 and 0.2 (Figure 2). It means, in x = 0.4, a faster ligand exchange taking place in bulk electrolyte and at the surface of electrode. The free G2 in the concentrated $AlCl_3$–G2 electrolyte has the least activity due to a faster formation of Al^{3+}–Cl–G2 complex,[1] even though the free G2 is still dominant with molar ratio of $[AlCl_2(G2)_2]^+$: $AlCl_4^-$: free G2 = 0.2 : 0.2 : 0.6. In the case of ILs and solvate ILs,[13-22] where free of neutral organic molecules, the Al is also deposited in the type of particles. Therefore, the concentrated $AlCl_3$–G2 electrolyte, where the activity of $AlCl_3$·G2 and G2 is effectively low, behaves like the ILs for Al electrodeposition. In contrast, a flake-like morphology is obtained in dilute $AlCl_3$–G2 electrolytes, where the $AlCl_3$·G2 and G2 have a higher activity. In particular, the size of particles in deposits obtained in the concentrated $AlCl_3$–G2 electrolyte is much smaller than those obtained in ILs and solvate ILs due to a different electrochemically active species.

Since the (111) plane has the lowest surface free energy in the case of the fcc metal like Al, the crystal is expected to grow preferentially along the <111> orientation. For

x = 0.1 and 0.2, likewise, the Al deposits are <111> oriented (Figure 5), which corresponds to the preferential outward growth, *i.e*. perpendicular to the substrate (Figure 6(a)-(c) and Figure S5 (Supporting Information)). However, the Al deposits obtained from x = 0.4 prefer a lateral growth, *i.e*. perpendicular to the substrate (Figure 6(d)). The difference between the outward and lateral growth is illustrated in Figure S11 (Supporting Information). Previous studies reveal that the crystal orientation of deposits is primarily determined by the aforementioned growth mode. Especially, the lateral growth of fcc metals always exhibits <100> preferential orientation.[67-69] Therefore, as for the concentrated $AlCl_3$–G2 electrolyte, the <100> oriented Al deposits (Figure 5) can be identified as the consequence of preferential lateral growth. Moreover, increasing the concentration of electrochemically active species will lead crystals to grow preferentially along the lateral direction rather than the outward direction.[69] In the concentrated $AlCl_3$–G2 electrolyte, the effectively low activity of neutral organic molecules and the maximum concentration of active species $[AlCl_2(G2)_2]^+$ are all in favor of the lateral growth of Al deposits. However, for the dilute $AlCl_3$–G2 electrolytes, as shown in Figure S11 (Supporting Information), the absorption of neutral organic molecules, *i.e*. $AlCl_3$·G2 complex and free G2, on the preferred growth sites suppresses the lateral growth of the Al deposits.

5. CONCLUSIONS

The concentrated $AlCl_3$–G2 electrolyte with a molar ratio x = 0.4 can be successfully

used for electrodeposition of aluminum with a void-free structure and smooth surface. By contrast, the Al deposits with micro-voids grow in a flake-like structure when the molar ratio of $AlCl_3$ is decreased. The Al deposits with a crystallite size of about 15 nm had a higher hardness than that of bulk Al with crystallite size about 1 μm, due to a Hall–Petch effect. The Al nuclei grow preferentially toward <100> direction for the x = 0.4. The compact microstructure together with <100> preferential orientation exhibit higher resistance to free corrosion and pitting corrosion. The nucleation mechanism of the Al deposits in $AlCl_3$–G2 electrolytes, as well as other interesting phenomena in the electrodeposited Al bulk-nanometal, will be clarified by detailed investigation in the future.

ASSOCIATED CONTENT

Supporting Information

Photographs of $AlCl_3$–G2 solutions; temperature dependence of viscosity and ionic conductivity; typical cyclic voltammetry; Al deposits obtained in the x = 0.43 electrolyte; SEM and XRD profiles of Al deposits obtained by galvanostatic electrodeposition; the cross-sectional TEM dark-field image of Al deposits obtained from the x = 0.1; the fitted parameters of the equivalent electrical circuit; Bode plots of Al deposits in 3.5 wt% NaCl solution; dark-field TEM image and HRTEM image of the Al deposits obtained from the x = 0.4; variation of yield stress with grain size for bulk Al and Al deposits; Schematic diagram of preferential outward and lateral growth.

(PDF)

AUTHOR INFORMATION

Corresponding Author

Atsushi Kitada – Department of Materials Science and Engineering, Kyoto University, Kyoto 606-8501, Japan; E-mail address: kitada.atsushi.3r@kyoto-u.ac.jp

Authors

Zelei Zhang – Department of Materials Science and Engineering, Kyoto University, Kyoto 606-8501, Japan; College of Materials Science and Technology, Nanjing University of Aeronautics and Astronautics, Nanjing 210016, China; ORCID ID 0000-0002-7035-1434

Si Gao – Department of Materials Science and Engineering, Kyoto University, Kyoto 606-8501, Japan; ORCID ID 0000-0002-6430-4172

Kazuhiro Fukami – Department of Materials Science and Engineering, Kyoto University, Kyoto 606-8501, Japan; ORCID ID 0000-0001-9120-5578

Nobuhiro Tsuji – Department of Materials Science and Engineering, Kyoto University, Kyoto 606-8501, Japan; ORCID ID 0000-0002-2132-1327

Zhengjun Yao – College of Materials Science and Technology, Nanjing University of Aeronautics and Astronautics, Nanjing 210016, China

Kuniaki Murase – Department of Materials Science and Engineering, Kyoto University, Kyoto 606-8501, Japan; ORCID ID 0000-0002-7564-9416

Notes

The authors declare no competing financial interest.

ACKNOWLEDGMENTS

This work was supported financially by Grants-in-Aid for Scientific Research (B) (No. 19H02490: A. K.) and Grant-in-Aid for Challenging Research (Exploratory) (No. 19K22056: A. K.) from the Japan Society for the Promotion of Science (JSPS). Z. Z. was financially supported by the China Scholarship Council (CSC, No. 201806830035) and the Open Fund of Key Laboratory of Material Preparation and Protection for Harsh Environment (56XCA17006-3).

REFERENCES

1. Yoshida, K.; Nakamura, M.; Kazue, Y.; Tachikawa, N.; Tsuzuki, S.; Seki, S.; Dokko, K.; Watanabe, M., Oxidative-Stability Enhancement and Charge Transport Mechanism in Glyme–Lithium Salt Equimolar Complexes. *J. Am. Chem. Soc.* **2011,** *133*, 13121-13129.
2. He, M.; Lau, K. C.; Ren, X.; Xiao, N.; McCulloch, W. D.; Curtiss, L. A.; Wu, Y., Concentrated Electrolyte for the Sodium–Oxygen Battery: Solvation Structure and Improved Cycle Life. *Angew. Chem. Int. Ed.* **2016,** *55*, 15310-15314.
3. Petibon, R.; Aiken, C.; Ma, L.; Xiong, D.; Dahn, J., The Use of Ethyl Acetate as a Sole Solvent in Highly Concentrated Electrolyte for Li-Ion Batteries. *Electrochim. Acta* **2015,** *154*, 287-293.
4. Adachi, K.; Kitada, A.; Fukami, K.; Murase, K., Cyanide-Free Displacement Silver Plating Using Highly Concentrated Aqueous Solutions of Metal Chloride Salts. *J. Electrochem. Soc.* **2019,** *166*, D409-D414.
5. Adachi, K.; Kitada, A.; Fukami, K.; Murase, K., Crystalline Chromium Electroplating with High Current Efficiency Using Chloride Hydrate Melt-Based Trivalent Chromium Baths. *Electrochim. Acta* **2020,** *338*, 135873.
6. Pavlović, M.; Kindlova, Š.; Roušar, I., The Initiation of Dendritic Growth of Electrodeposited Copper on a Rotating Disc Electrode with Changing Copper Concentration and Diffusion Layer Thickness. *Electrochim. Acta* **1992,** *37*, 23-27.
7. da Silva, F. S.; Bedoya, J.; Dosta, S.; Cinca, N.; Cano, I. G.; Guilemany, J. M.; Benedetti, A. V., Corrosion Characteristics of Cold Gas Spray Coatings of Reinforced Aluminum Deposited onto Carbon Steel. *Corros. Sci.* **2017,** *114*, 57-71.
8. Wang, S.; Yu, Z. J.; Tu, J. G.; Wang, J. X.; Tian, D. H.; Liu, Y. J.; Jiao, S. Q., A Novel Aluminum-Ion Battery: Al/$AlCl_3$-[Emim]Cl/Ni_3S_2@Graphene. *Adv. Energy Mater.* **2016,** *6*.
9. Lin, M. C.; Gong, M.; Lu, B. G.; Wu, Y. P.; Wang, D. Y.; Guan, M. Y.; Angell, M.; Chen, C. X.; Yang, J.; Hwang, B. J.; Dai, H. J., An Ultrafast Rechargeable Aluminium-Ion Battery. *Nature* **2015,** *520*, 324-328.
10. Li, H.; Yamaguchi, T.; Matsumoto, S.; Hoshikawa, H.; Kumagai, T.; Okamoto, N. L.; Ichitsubo, T., Circumventing Huge Volume Strain in Alloy Anodes of Lithium Batteries. *Nature Communications* **2020,** *11*, 1-8.
11. Chang, X.; Xie, Z.; Liu, Z.; Zheng, X.; Zheng, J.; Li, X., Aluminum: An Underappreciated Anode Material for Lithium-Ion Batteries. *Energy Storage Mater.* **2020,** *25*, 93-99.
12. Jafarian, M.; Mahjani, M. G.; Gobal, F.; Danaee, I., Electrodeposition of Aluminum from Molten $AlCl_3$-NaCl-KCl Mixture. *J. Appl. Electrochem.* **2006,** *36*, 1169-1173.
13. Jiang, T.; Brym, M. J. C.; Dube, G.; Lasia, A.; Brisard, G. M., Electrodeposition of Aluminium from Ionic Liquids: Part I - Electrodeposition and Surface Morphology of Aluminium from Aluminium Chloride ($AlCl_3$)-1-Ethyl-3-Methylimidazolium Chloride ([Emim]Cl) Ionic Liquids. *Surf. Coat. Technol.* **2006,** *201*, 1-9.
14. Yue, G.; Lu, X.; Zhu, Y.; Zhang, X.; Zhang, S., Surface Morphology, Crystal

Structure and Orientation of Aluminium Coatings Electrodeposited on Mild Steel in Ionic Liquid. *Chem. Eng. J.* **2009,** *147*, 79-86.
15. Caporali, S.; Fossati, A.; Lavacchi, A.; Perissi, I.; Tolstogouzov, A.; Bardi, U., Aluminium Electroplated from Ionic Liquids as Protective Coating against Steel Corrosion. *Corros. Sci.* **2008,** *50*, 534-539.
16. Chang, J. K.; Chen, S. Y.; Tsai, W. T.; Deng, M. J.; Sun, I. W., Electrodeposition of Aluminum on Magnesium Alloy in Aluminum Chloride ($AlCl_3$)-1-Ethyl-3-Methylimidazolium Chloride (EMIC) Ionic Liquid and Its Corrosion Behavior. *Electrochem. Commun.* **2007,** *9*, 1602-1606.
17. Yang, H.; Guo, X.; Wu, G.; Ding, W.; Birbilis, N., Electrodeposition of Chemically and Mechanically Protective Al-Coatings on AZ91D Mg Alloy. *Corros. Sci.* **2011,** *53*, 381-387.
18. Li, M.; Gao, B.; Liu, C.; Chen, W.; Shi, Z.; Hu, X.; Wang, Z., Electrodeposition of Aluminum from $AlCl_3$/Acetamide Eutectic Solvent. *Electrochim. Acta* **2015,** *180*, 811-814.
19. Abbott, A. P.; Harris, R. C.; Hsieh, Y. T.; Ryder, K. S.; Sun, I. W., Aluminium Electrodeposition under Ambient Conditions. *Phys. Chem. Chem. Phys.* **2014,** *16*, 14675-14681.
20. Endo, A.; Miyake, M.; Hirato, T., Electrodeposition of Aluminum from 1, 3-Dimethyl-2-Imidazolidinone/$AlCl_3$ Baths. *Electrochim. Acta* **2014,** *137*, 470-475.
21. Fang, Y. X.; Jiang, X. G.; Sun, X. G.; Dai, S., New Ionic Liquids Based on the Complexation of Dipropyl Sulfide and $AlCl_3$ for Electrodeposition of Aluminum. *Chem. Commun.* **2015,** *51*, 13286-13289.
22. Fang, Y.; Yoshii, K.; Jiang, X.; Sun, X.-G.; Tsuda, T.; Mehio, N.; Dai, S., An $AlCl_3$ Based Ionic Liquid with a Neutral Substituted Pyridine Ligand for Electrochemical Deposition of Aluminum. *Electrochim. Acta* **2015,** *160*, 82-88.
23. Tsuda, T.; Stafford, G. R.; Hussey, C. L., Electrochemical Surface Finishing and Energy Storage Technology with Room-Temperature Haloaluminate Ionic Liquids and Mixtures. *J. Electrochem. Soc.* **2017,** *164*, H5007-H5017.
24. Ishibashi, N.; Yoshio, M., Electrodeposition of Aluminium from the NBS Type Bath Using Tetrahydrofuran-Benzene Mixed Solvent. *Electrochim. Acta* **1972,** *17*, 1343-1352.
25. Peled, E.; Gileadi, E., The Electrodeposition of Aluminum from Aromatic Hydrocarbon: I. Composition of Baths and the Effect of Additives. *J. Electrochem. Soc.* **1976,** *123*, 15.
26. Couch, D. E.; Brenner, A., A Hydride Bath for the Electrodeposition of Aluminum. *J. Electrochem. Soc.* **1952,** *99*, 234.
27. Kitada, A.; Nakamura, K.; Fukami, K.; Murase, K., $AlCl_3$-Dissolved Diglyme as Electrolyte for Room-Temperature Aluminum Electrodeposition. *Electrochemistry* **2014,** *82*, 946-948.
28. Kitada, A.; Nakamura, K.; Fukami, K.; Murase, K., Electrochemically Active Species in Aluminum Electrodeposition Baths of $AlCl_3$/Glyme Solutions. *Electrochim. Acta* **2016,** *211*, 561-567.
29. Kitada, A.; Kato, Y.; Fukami, K.; Murase, K., Room Temperature

Electrodeposition of Flat and Smooth Aluminum Layers from an $AlCl_3$/Diglyme Bath. *J. Surf. Finish. Soc. Jpn.* **2018,** *69*, 310-311.
30. Zhang, Z. L.; Kitada, A.; Chen, T. Y.; Fukami, K.; Shimizu, M.; Arai, S.; Yao, Z. J.; Murase, K., Dispersion of Multiwalled Carbon Nanotubes into a Diglyme Solution, Electrodeposition of Aluminum-Based Composite, and Improvement of Hardness. *J. Alloys Compd.* **2020,** *816*.
31. Zhang, Z.; Kitada, A.; Fukami, K.; Yao, Z.; Murase, K., Electrodeposition of an Iron Thin Film with Compact and Smooth Morphology Using an Ethereal Electrolyte. *Electrochim. Acta* **2020,** *348*, 136289.
32. Reed, L. D.; Arteaga, A.; Menke, E. J., A Combined Experimental and Computational Study of an Aluminum Triflate/Diglyme Electrolyte. *J. Phys. Chem. B* **2015,** *119*, 12677-12681.
33. Mandai, T.; Johansson, P., Al Conductive Haloaluminate-Free Non-Aqueous Room-Temperature Electrolytes. *J. Mater. Chem. A* **2015,** *3*, 12230-12239.
34. Tang, S.; Zhao, H., Glymes as Versatile Solvents for Chemical Reactions and Processes: From the Laboratory to Industry. *RSC Adv.* **2014,** *4*, 11251-11287.
35. Wu, Y. C.; Koch, W. F., Absolute Determination of Electrolytic Conductivity for Primary Standard KCl Solutions from 0 to 50 °C. *J. Solution Chem.* **1991,** *20*, 391-401.
36. Chavez, K. L.; Hess, D. W., A Novel Method of Etching Copper Oxide Using Acetic Acid. *J. Electrochem. Soc.* **2001,** *148*, G640-G643.
37. Oliver, W. C.; Pharr, G. M., An Improved Technique for Determining Hardness and Elastic-Modulus Using Load and Displacement Sensing Indentation Experiments. *J. Mater. Res.* **1992,** *7*, 1564-1583.
38. Nöth, H.; Rurländer, R.; Wolfgardt, P., An Investigation of $AlCl_3$ Solutions in Ethers by ^{27}Al NMR Spectroscopy. *Z. Naturforsch., B: Chem. Sci.* **1982,** *37*, 29-37.
39. Coleman, F.; Srinivasan, G.; Swadźba - Kwaśny, M., Liquid Coordination Complexes Formed by the Heterolytic Cleavage of Metal Halides. *Angew. Chem. Int. Ed.* **2013,** *52*, 12582-12586.
40. Pulletikurthi, G.; Bodecker, B.; Borodin, A.; Weidenfeller, B.; Endres, F., Electrodeposition of Al from a 1-Butylpyrrolidine-$AlCl_3$ Ionic Liquid. *Prog. Nat. Sci.* **2015,** *25*, 603-611.
41. Kitada, A.; Takeoka, S.; Kintsu, K.; Fukami, K.; Saimura, M.; Nagata, T.; Katahira, M.; Murase, K., A Hydronium Solvate Ionic Liquid: Facile Synthesis of Air-Stable Ionic Liquid with Strong Bronsted Acidity. *J. Electrochem. Soc.* **2018,** *165*, H121-H127.
42. Schreiner, C.; Zugmann, S.; Hartl, R.; Gores, H. J., Fractional Walden Rule for Ionic Liquids: Examples from Recent Measurements and a Critique of the So-Called Ideal KCl Line for the Walden Plot. *J. Chem. Eng. Data* **2010,** *55*, 1784-1788.
43. Kawata, K.; Kitada, A.; Tsuchida, N.; Saimura, M.; Nagata, T.; Katahira, M.; Fukami, K.; Murase, K., Suppression of Fast Proton Conduction by Dilution of a Hydronium Solvate Ionic Liquid: Localization of Ligand Exchange. *J. Electrochem. Soc.* **2020,** *167*, 046508.
44. Matsui, I.; Hanaoka, Y.; Ono, S.; Takigawa, Y.; Uesugi, T.; Higashi, K., Pre-Electrodeposition Process for Improving Tensile Ductility of Al Electrodeposited from a Dimethylsulfone Bath. *Mater. Lett.* **2013,** *109*, 229-232.

45. Matsui, I.; Ono, S.; Takigawa, Y.; Uesugi, T.; Higashi, K., Fabrication of Bulk Nanocrystalline Al Electrodeposited from a Dimethylsulfone Bath. *Mater. Sci. Eng., A* **2012,** *550*, 363-366.
46. Miyake, M.; Motonami, H.; Shiomi, S.; Hirato, T., Electrodeposition of Purified Aluminum Coatings from Dimethylsulfone–$AlCl_3$ Electrolytes with Trimethylamine Hydrochloride. *Surf. Coat. Technol.* **2012,** *206*, 4225-4229.
47. Zhang, L.; Ohmura, T.; Emura, S.; Sekido, N.; Yin, F.; Min, X.; Tsuzaki, K., Evaluation of Matrix Strength in Ultra-Fine Grained Pure Al by Nanoindentation. *J. Mater. Res.* **2009,** *24*, 2917-2923.
48. Rafailović, L. D.; Gammer, C.; Ebner, C.; Rentenberger, C.; Jovanović, A. Z.; Pašti, I. A.; Skorodumova, N. V.; Karnthaler, H. P., High Density of Genuine Growth Twins in Electrodeposited Aluminum. *Sci. Adv.* **2019,** *5*, eaax3894.
49. Prakashaiah, B. G.; Kumara, D. V.; Pandith, A. A.; Shetty, A. N.; Rani, B. E. A., Corrosion Inhibition of 2024-T3 Aluminum Alloy in 3.5% NaCl by Thiosemicarbazone Derivatives. *Corros. Sci.* **2018,** *136*, 326-338.
50. Trdan, U.; Grum, J., Evaluation of Corrosion Resistance of AA6082-T651 Aluminium Alloy after Laser Shock Peening by Means of Cyclic Polarisation and ElS Methods. *Corros. Sci.* **2012,** *59*, 324-333.
51. Trueba, M.; Trasatti, S. P., Study of Al Alloy Corrosion in Neutral NaCl by the Pitting Scan Technique. *Mater. Chem. Phys.* **2010,** *121*, 523-533.
52. Yasuda, M.; Weinberg, F.; Tromans, D., Pitting Corrosion of Al and Al-Cu Single-Crystals. *J. Electrochem. Soc.* **1990,** *137*, 3708-3715.
53. Amin, M. A.; Refat, M. S., Study of Complex Formation in Al(III)–Gluconic Acid System and the Influence of UV Light on the Dissolution and Passive Behavior of Al. *Arabian J. Chem.* **2013,** *6*, 165-172.
54. Cordero, Z. C.; Knight, B. E.; Schuh, C. A., Six Decades of the Hall–Petch Effect–a Survey of Grain-Size Strengthening Studies on Pure Metals. *Int. Mater. Rev.* **2016,** *61*, 495-512.
55. Meyers, M. A.; Mishra, A.; Benson, D. J., Mechanical Properties of Nanocrystalline Materials. *Prog. Mater Sci.* **2006,** *51*, 427-556.
56. Liu, M.; Lu, C.; Tieu, K. A.; Peng, C.-T.; Kong, C., A Combined Experimental-Numerical Approach for Determining Mechanical Properties of Aluminum Subjects to Nanoindentation. *Sci. Rep.* **2015,** *5*, 15072.
57. Kamikawa, N.; Huang, X.; Tsuji, N.; Hansen, N., Strengthening Mechanisms in Nanostructured High-Purity Aluminium Deformed to High Strain and Annealed. *Acta Mater.* **2009,** *57*, 4198-4208.
58. Kamikawa, N. PhD thesis, Osaka University, Japan, 2006.
59. Hu, J.; Shi, Y.; Sauvage, X.; Sha, G.; Lu, K., Grain Boundary Stability Governs Hardening and Softening in Extremely Fine Nanograined Metals. *Science* **2017,** *355*, 1292-1296.
60. Barnoush, A., Correlation between Dislocation Density and Nanomechanical Response During Nanoindentation. *Acta Mater.* **2012,** *60*, 1268-1277.
61. Tsuji, N.; Ito, Y.; Saito, Y.; Minamino, Y., Strength and Ductility of Ultrafine Grained Aluminum and Iron Produced by ARB and Annealing. *Scripta Mater.* **2002,**

47, 893-899.
62. Komanduri, R.; Chandrasekaran, N.; Raff, L., MD Simulation of Indentation and Scratching of Single Crystal Aluminum. *Wear* **2000,** *240*, 113-143.
63. Lehoczky, S., Strength Enhancement in Thin-Layered Al-Cu Laminates. *J. Appl. Phys.* **1978,** *49*, 5479-5485.
64. Martinson, C. W. B.; Flodstrom, S. A., Oxygen-Adsorption on Aluminum Single-Crystal Faces Studies by AES, XPS and LEED. *Surf. Sci.* **1979,** *80*, 306-316.
65. Tang, J.; Azumi, K., Optimization of Pulsed Electrodeposition of Aluminum from $AlCl_3$-1-Ethyl-3-Methylimidazolium Chloride Ionic Liquid. *Electrochim. Acta* **2011,** *56*, 1130-1137.
66. Chandrasekar, M.; Malathy, P., Synergetic Effects of Pulse Constraints and Additives in Electrodeposition of Nanocrystalline Zinc: Corrosion, Structural and Textural Characterization. *Mater. Chem. Phys.* **2010,** *124*, 516-528.
67. Finch, G.; Wilman, H.; Yang, L., Crystal Growth at the Cathode. *Discuss. Faraday Soc.* **1947,** *1*, 144-158.
68. Lin, C.; Hsu, P.; Chang, L.; Chen, C., Properties and Microstructure of Nickel Electrodeposited from a Sulfamate Bath Containing Ammonium Ions. *J. Appl. Electrochem.* **2001,** *31*, 925-933.
69. Banerjee, B.; Goswami, u. A., The Structure of Electro - Deposited Nickel. *J. Electrochem. Soc.* **1959,** *106*, 20-23.

Table of Contents